

# Accumulation phenomenon of dipole-dipole interaction induced by dark Rydberg atoms

Ko-Tang Chen,<sup>1</sup> Bongjune Kim,<sup>1,\*</sup> Chia-Chen Su,<sup>1</sup> Shih-Si

Hsiao,<sup>1</sup> Shou-Jou Huang,<sup>2</sup> Wen-Te Liao,<sup>2,3,4</sup> and Ite A. Yu,<sup>1,4,†</sup>

<sup>1</sup>*Department of Physics, National Tsing Hua University, Hsinchu 30013, Taiwan*

<sup>2</sup>*Department of Physics, National Central University, Taoyuan City 320317, Taiwan*

<sup>3</sup>*Physics Division, National Center for Theoretical Sciences, Taipei 10617, Taiwan*

<sup>4</sup>*Center for Quantum Technology, Hsinchu 30013, Taiwan*

We experimentally observed an accumulative type of nonlinear attenuation and distortion of slow light in a laser-cooled electromagnetically-induced-transparency (EIT) medium with the Rydberg state of  $|32D_{5/2}\rangle$ . The present effect of attenuation and distortion was caused by the dipole-dipole interaction between Rydberg atoms in a weak-interaction regime, i.e., the mean distance between Rydberg atoms was far greater than the dipole blockade radius. Our observation can be attributed to the atoms self-accumulated in dark Rydberg states other than those in the bright Rydberg state  $|32D_{5/2}\rangle$  driven by the coupling field. We performed three different experiments to verify the above hypothesis, to confirm the existence of the dark Rydberg states, and to measure the decay rate from the bright to dark Rydberg states. In the theoretical model, we included the decay process from the bright to dark Rydberg states and the DDI effect induced by both the bright and dark Rydberg atoms. All the experimental data of slow light taken at various probe Rabi frequencies were in good agreement with the theoretical predictions based on the model. The systematic study presented in this work provides a better understanding of the Rydberg-EIT system.

## I. INTRODUCTION

Atoms in the Rydberg states possess a strong electric dipole-dipole interaction (DDI) among themselves. The blockade effect arising from the DDI is a versatile mechanism for quantum information processing [1–4]. The combination of the DDI and the effect of electromagnetically induced transparency (EIT) can mediate strong photon-photon interactions [5–12]. Thus, Rydberg atoms have led to applications such as quantum logic gates [5, 13–15], single-photon generation [16–18], single-photon transistors [6, 7], and single-photon switches [8]. Furthermore, the system of Rydberg atoms in a vapor or an array is also a platform for the study of many-body physics [19–26].

Most of the experimental studies on Rydberg atoms have been performed in a strong interaction regime. In this work, we experimentally studied the DDI-induced effect in a weak interaction regime, i.e.,  $(r_B/r_a)^3 < 0.06$  where  $r_a$  is the half mean distance between the Rydberg atoms, and  $r_B$  is the blockade radius. The Rydberg state with a low principal quantum number of  $n = 32$  and a low Rydberg-atom density equal to or less than  $2.0 \times 10^9 \text{ cm}^{-3}$  were employed in the experiment. Nevertheless, a high optical depth (OD) equal to or larger than 70 and a low decoherence rate of  $2\pi \times 49 \text{ kHz}$  in the experimental system enabled us to observe the DDI-induced effect in the weak interaction regime [27, 28]. Due to the EIT effect [29], the propagation delay time or photon-matter interaction time in our high-OD medium was a

couple of  $\mu\text{s}$ . The high-OD EIT medium of weakly interacting Rydberg atoms can lead to realization of Bose-Einstein condensation of Rydberg polaritons [28].

In this work, we systematically studied the transmission of a probe field propagating through a Rydberg-EIT system, in which the Rydberg state of  $|32D_{5/2}\rangle$  was employed. The probe field drove the transition from the ground state of  $|5S_{1/2}\rangle$  to the intermediate state of  $|5P_{3/2}\rangle$ , while the coupling field drove the transition from the intermediate state to the Rydberg states. Both the probe and coupling frequencies were nearly resonant to the transitions, and the two-photon resonance condition was accurately maintained. With a weak and short Gaussian probe pulse, the propagation delay time of the pulse was about  $1.8 \mu\text{s}$  under the coupling Rabi frequency,  $\Omega_c$ , of  $1.0\Gamma$ . The experimental data of the output probe pulse was in agreement with the theoretical prediction. However, when we employed a long Gaussian input probe pulse, the output pulse was distorted and the experimental data were inconsistent with the theoretical prediction, in which the DDI-induced decoherence rate was considered. A larger input probe Rabi frequency,  $\Omega_{p0}$ , resulted in a more severe distortion, while the condition of  $\Omega_{p0}^2 \ll \Omega_c^2$  was always satisfied. The distortion phenomenon of the long Gaussian pulse was unexpected.

To investigate the distortion phenomenon, we employed a quasi-continuous wave (CW) probe field and measured its output transmission. It was expected from the theoretical prediction that the transmission should increase to a steady-state value. However, experimentally, the transmission reached the maximum and then decayed to a steady-state value. A larger value of  $\Omega_{p0}$  resulted in a faster decay and a lower steady-state transmission. To explain the unexpected decay behavior of the transmission, we suggest that the DDI-induced de-

\*Electronic address: upfe11@gmail.com

†Electronic address: yu@phys.nthu.edu.tw

coherence rate,  $\gamma_{\text{DDI}}$ , or the DDI strength increases over time.

After the quasi-CW probe field was switched off, we further applied a very weak Gaussian probe pulse to measure  $\gamma_{\text{DDI}}$  of the system at a lag time. The coupling field remained unchanged during the measurement, and quickly removed the population in  $|32D_{5/2}\rangle$ . Since the weak probe pulse produced little DDI, one could expect that  $\gamma_{\text{DDI}}$  would also quickly decrease to nearly zero after the quasi-CW probe field was switched off. On the contrary,  $\gamma_{\text{DDI}}$  slowly decreased to an insignificant value with a decay time constant that was close to the lifetimes of the Rydberg states, with  $n$  around 32. This observation suggested that after the quasi-CW probe field was switched off, the population still remained in some Rydberg states and was not de-excited by the coupling field. As these Rydberg states were not driven by the coupling field, we call them dark Rydberg states. Similarly,  $|32D_{5/2}\rangle$  is called the bright Rydberg state.

In the measurements of the long Gaussian probe pulse and quasi-CW probe field, atoms in the bright Rydberg state were able to be transferred to those in the dark Rydberg states. Possible transfer processes will be discussed in the Discussion section. Since not interacting with the coupling field, the dark Rydberg atoms accumulated over time. On the other hand, the DDI between the dark and bright Rydberg atoms existed. A larger number or density of the dark Rydberg atoms produced a larger DDI on the bright Rydberg atoms. Consequently, the probe light suffered a larger DDI-induced decoherence rate in the EIT system consisting of the bright Rydberg state. As the dark Rydberg atoms accumulated over time, the DDI-induced decoherence rate increased with time. The above description can explain the phenomena observed with the long Gaussian probe pulse and the quasi-CW probe field.

To quantitatively study the accumulation phenomenon, we modified the optical Bloch equations (OBEs) to include the process of the population transfer from the bright to dark Rydberg states and took into account the DDI-induced decoherence rate due to the population in the dark Rydberg states. We also measured the transfer or decay rate of the atoms from the bright to dark Rydberg states. The measured decay rate was linearly proportional to the density of the bright Rydberg atoms. We modeled the decay process in the OBEs and set the parameters of the decay rate according to the experimental result. In addition, the DDI-induced decoherence rate due to the population in the dark Rydberg states was determined by the experimental data of the quasi-CW probe field. Finally, we compared the experimental data of the distorted output probe pulse taken at different values of  $\Omega_{p0}$  with the theoretical predictions, which were calculated from the modified OBEs without any adjustable parameters. The theoretical predictions were in good agreements with the experimental data. Thus, the distortion of the output probe pulse in the Rydberg-EIT system was well understood.

This article is organized as follows. In Sec. II, we present the distorted output probe pulse shapes, which we cannot explain with the theoretical model as it only considered the DDI between the bright Rydberg states under the EIT condition. In addition, we show the necessity of the consideration of the dark Rydberg states by measurements of the decay time constant, the steady-state attenuation coefficient of the square input pulse, and the lifetime of the dark Rydberg state. In Sec. III, we introduce a modified theoretical model to describe the increasing attenuation coefficient over time depending on the density of the Rydberg atom. We also report the method for estimating the decay rate from the bright Rydberg state to the dark Rydberg state and compare the experimental data with the theoretical prediction. In Sec. IV, we discuss the possible transfer process from the bright to the dark Rydberg states. Finally, we summarize the results in Sec. V.

## II. OBSERVATION OF THE ACCUMULATION EFFECT

### A. Experiment setup

The experiment was performed with a cigar-shaped cold  $^{87}\text{Rb}$  atom cloud produced by a magneto-optical trap. The dimension of the cloud was  $1.5 \times 1.5 \times 5.0 \text{ mm}^3$  [30] and the temperature was about  $350 \mu\text{K}$  [28, 31]. The transition scheme formed by the probe and coupling fields is shown in Fig. 1(a). The probe field drove the transition between the ground state  $|1\rangle$  and the intermediate state  $|3\rangle$ , and the coupling field drove the transition between state  $|3\rangle$  and the Rydberg state  $|2\rangle$ . States  $|1\rangle$ ,  $|2\rangle$ , and  $|3\rangle$  corresponded to the ground state  $|5S_{1/2}, F=2, m_F=2\rangle$ , the Rydberg state  $|32D_{5/2}, m_J=5/2\rangle$ , and the excited state  $|5P_{3/2}, F=3, m_F=3\rangle$  of  $^{87}\text{Rb}$  atoms, respectively. We prepared all population in a single Zeeman state  $|5S_{1/2}, F=2, m_F=2\rangle$  by optical pumping [32]. In the experiment, the  $\sigma_+$ -polarized probe and coupling fields were used. Owing to the optical pumping and polarization of the laser fields, the relevant energy levels  $|1\rangle$ ,  $|2\rangle$ , and  $|3\rangle$  were considered as a single Zeeman state. The spontaneous decay rate of  $|3\rangle$  is  $\Gamma = 2\pi \times 6.07 \text{ MHz}$ , and that of  $|2\rangle$  is  $\Gamma_2 = 2\pi \times 7.9 \text{ kHz}$  or  $1.3 \times 10^{-3} \Gamma$  [33, 34]. As the van der Waals interaction energy is denoted as  $\hbar C_6/r^6$ , the Rydberg atoms in  $|32D_{5/2}, m_J=5/2\rangle$  have  $C_6 = -2\pi \times 130 \text{ MHz} \cdot \mu\text{m}^6$  [35].

The experimental scheme is shown in Fig. 1(b). Frequency stabilized laser systems generated the probe and coupling fields. The details of the stabilization method are described in Refs. [28, 31]. The probe and coupling fields were the first-order beams of the acousto-optic modulators (AOMs, not drawn in the figure). The AOMs were used to control the time sequence, shape the probe pulse, and adjust the frequency and the amplitude of the fields precisely. Each field was sent to the atom cloud by the polarization maintained optical fiber

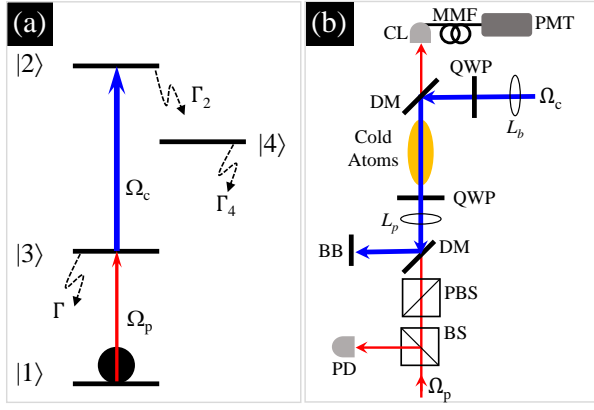


FIG. 1: (a) Relevant energy levels and transitions of the laser fields.  $|1\rangle$  and  $|3\rangle$  are the ground and intermediate excited states.  $|2\rangle$  is the Rydberg state driven by the coupling field, and  $|4\rangle$  represents all the nearby Rydberg states of  $|2\rangle$  that involve the DDI effect.  $|2\rangle$  and  $|4\rangle$  are the bright and dark Rydberg states, respectively.  $\Gamma$ ,  $\Gamma_2$ , and  $\Gamma_4$  represent the spontaneous decay rates of  $|3\rangle$ ,  $|2\rangle$ , and  $|4\rangle$ .  $\Omega_p$  and  $\Omega_c$  denote the Rabi frequencies of the probe and coupling fields. The two fields' frequencies were stabilized to maintain the two-photon resonance. As compared with  $\Gamma$ , the magnitude of the one-photon detuning was negligible. (b) Sketch of the experiment setup. BS: beam splitter; PBS: polarizing beam splitter; PD: photo detector; DM: dichroic mirror;  $L_p$ ,  $L_b$ : lenses; QWP: quarter-wave plate; CL: collimation lens; MMF: multimode optical fiber; PMT: photomultiplier tube. Red and blue arrowed lines indicate the optical paths of the probe and coupling beams.

(PMF) after the AOM. To minimize the Doppler effect, we used the counter-propagating scheme of the probe and coupling fields. At the center of the cloud, the  $e^{-1}$  full widths of the probe and coupling beams were 130 and 250  $\mu\text{m}$ , respectively. The pulse shape and amplitude of the input probe field were monitored by a photo detector (PD) before entering the atom cloud as shown in Fig. 1(b). The probe field was detected by a photomultiplier tube (PMT) after passing through the atom cloud. A digital oscilloscope (Agilent MSO6014A) acquired the signal from the PMT and produced the raw data.

### B. Theoretical model without the accumulation effect

The Rydberg atoms inside the cloud were considered randomly distributed particles, similar to ideal gases, due to the assumption that the condition of a weakly-interacting many-body system of Rydberg polaritons was satisfied. Therefore, the mean-field model developed in Ref. [27] was adopted to describe the DDI-induced behaviors in this study.

We initially considered only the states  $|1\rangle$ ,  $|2\rangle$ , and  $|3\rangle$  shown by Fig. 1(a) in the theoretical model. The DDI-induced decoherence rate ( $\gamma_{\text{DDI}}$ ) and frequency shift

( $\delta_{\text{DDI}}$ ), which are caused by the population in the Rydberg state  $|2\rangle$ , were taken into account. The optical Bloch equations (OBEs) of the density matrix operator and the Maxwell-Schrödinger equation (MSE) of the probe field are given below:

$$\frac{\partial}{\partial t}\rho_{21} = \frac{i}{2}\Omega_c\rho_{31} + i(\delta_{\text{DDI}} + \delta)\rho_{21} - \left(\gamma_{\text{DDI}} + \gamma_0 + \frac{\Gamma_2}{2}\right)\rho_{21}, \quad (1)$$

$$\frac{\partial}{\partial t}\rho_{31} = \frac{i}{2}\Omega_p(\rho_{11} - \rho_{33}) + \frac{i}{2}\Omega_c\rho_{21} + i\Delta_p\rho_{31} - \frac{\Gamma}{2}\rho_{31}, \quad (2)$$

$$\frac{\partial}{\partial t}\rho_{32} = \frac{i}{2}\Omega_p\rho_{21}^* + \frac{i}{2}\Omega_c(\rho_{22} - \rho_{33}) - i\Delta_c\rho_{32} - \frac{\Gamma}{2}\rho_{32}, \quad (3)$$

$$\frac{\partial}{\partial t}\rho_{22} = \frac{i}{2}\Omega_c\rho_{32} - \frac{i}{2}\Omega_c\rho_{32}^* - \Gamma_2\rho_{22}, \quad (4)$$

$$\frac{\partial}{\partial t}\rho_{33} = -\frac{i}{2}\Omega_p^*\rho_{31} + \frac{i}{2}\Omega_p\rho_{31}^* - \frac{i}{2}\Omega_c\rho_{32} + \frac{i}{2}\Omega_c\rho_{32}^* - \Gamma\rho_{33}, \quad (5)$$

$$\frac{\partial}{\partial t}\rho_{11} = \frac{i}{2}\Omega_p^*\rho_{31} - \frac{i}{2}\Omega_p\rho_{31}^* + \Gamma\rho_{33} \quad (6)$$

$$\frac{1}{c}\frac{\partial}{\partial t}\Omega_p + \frac{\partial}{\partial z}\Omega_p = i\frac{\alpha\Gamma}{2L}\rho_{31}, \quad (7)$$

where  $\rho_{ij}$  ( $i, j = 1, 2, 3$ ) represents a matrix element of the density matrix operator,  $\Omega_p$  and  $\Omega_c$  are the Rabi frequencies of the probe and coupling fields,  $\delta$  is the two-photon detuning,  $\gamma_0$  is the intrinsic decoherence rate in the experimental system,  $\Delta_p$  and  $\Delta_c$  are the one-photon detunings of the probe and coupling transitions, and  $\alpha$  and  $L$  are the optical depth and length of the medium.

The values of  $\gamma_{\text{DDI}}$  and  $\delta_{\text{DDI}}$  were obtained by the analytic formulas of the attenuation coefficient ( $\Delta\beta$ ) and the phase shift ( $\Delta\phi$ ), respectively, induced by the DDI in the steady-state condition. The formulas were derived in Ref. [27], utilizing a mean-field model based on the nearest neighbor distribution, and they were experimentally verified in Ref. [28]. At the condition of  $\delta = 0$  and  $\Delta_c \ll \Gamma$ , the formulas of  $\Delta\beta$  and  $\Delta\phi$  are given by:

$$\Delta\beta \left( \equiv \frac{2\alpha\Gamma\gamma_{\text{DDI}}}{\Omega_c^2} \right) = \frac{2\pi^2\alpha\sqrt{|C_6|}\Gamma}{3\Omega_c}n_R, \quad (8)$$

$$\Delta\phi \left( \equiv \frac{\alpha\Gamma\delta_{\text{DDI}}}{\Omega_c^2} \right) = \frac{\pi^2\alpha\sqrt{|C_6|}\Gamma}{3\Omega_c}n_R, \quad (9)$$

where  $n_R$  is the density of the Rydberg-state atoms. Using the relation  $n_R = n_a\rho_{22}$  between  $n_R$  and the density of all atoms,  $n_a$ , we introduced the coefficient  $A$ , which is written as:

$$A = \frac{\pi^2\Omega_c\sqrt{|C_6|}}{3\sqrt{\Gamma}}n_a. \quad (10)$$

The coefficient  $A$  represents the DDI-induced decoherence rate or frequency shift per unit  $\rho_{22}$ . From Eqs. (8) and (10), we obtained:

$$\gamma_{\text{DDI}} = A\rho_{22}. \quad (11)$$

Similarly, from Eqs. (9) and (10), we also obtained:

$$\delta_{\text{DDI}} = A\rho_{22}. \quad (12)$$

Thus,  $\gamma_{\text{DDI}}$  and  $\delta_{\text{DDI}}$  were replaced by  $A\rho_{22}$  in the OBEs. According to the values of  $\Omega_c$ ,  $C_6$ , and  $n_a$  used in the experiment, it was determined that  $A = 0.76\Gamma$ . We set and fixed  $A$  to  $0.76\Gamma$  in all the theoretical predictions of this work and the values of  $\gamma_{\text{DDI}}$  and  $\delta_{\text{DDI}}$  are linearly proportional to the population of the Rydberg state,  $\rho_{22}(z, t)$ .

Furthermore, the effect of the DDI, i.e.,  $\gamma_{\text{DDI}}$  and  $\delta_{\text{DDI}}$ , was ignored to obtain Eq. (3) due to the assumption of  $A\rho_{22}, \Gamma_2 \ll \Gamma$ , which was the case in the experiment. Throughout this study, the two-photon resonance condition of  $\delta (\equiv \Delta_p + \Delta_c) = 0$  was always maintained. Please note that the term of  $i(\delta_{\text{DDI}} + \delta)\rho_{21}$  in Eq. (1), i.e.,  $i(A\rho_{22} + \delta)\rho_{21}$ , played a negligible role in the output probe transmission, since  $\delta = 0$  and  $4(A\rho_{22})^2\Gamma^2 \ll \Omega_c^4$  in all the cases of this work. To obtain Eqs. (5) and (6), we also considered that the population in  $|2\rangle$  rarely decayed to  $|1\rangle$  and  $|3\rangle$ . When we made the population in  $|2\rangle$  all decay to  $|1\rangle$  by adding the term of  $+\Gamma_2\rho_{22}$  to the right-hand-side of Eq. (6), the calculation result changed very little because  $\Omega_p^2 \ll \Omega_c^2$  in this work.

### C. Distorted output pulses of slow light

Before the measurement, the values of the one-photon detuning and two-photon detuning were set to zero and experimentally verified. We determined the experimental parameters in the order of  $\Omega_c \rightarrow \gamma_0 \rightarrow \text{OD}$ . The parameters were confirmed again after the measurement in the reverse order of that before measurement. To measure the values of  $\Omega_c$  and  $\gamma_0$ , we intentionally reduced the OD to a value between 15 and 20 by adjusting the dark MOT parameter to minimize the effect of DDI. The measurement results enabled us to set and verify  $\Omega_c = 1.0\Gamma$  and determine  $\gamma_0 = 8.0 \times 10^{-3}\Gamma$ . Then, we employed a short and weak Gaussian probe pulse to determine the OD by the delay time. The pulse was sufficiently weak such that the DDI effect played a negligible role in the delay time. It was determined that  $\alpha$  (OD) = 70 in the experiment. The detailed methods are described in Ref. [31]. Following the definition of the half mean distance between Rydberg polaritons,  $r_a = (4\pi n_R/3)^{-1/3}$ , the estimated smallest  $r_a$  in this experiment was  $5.0 \mu\text{m}$  when  $\Omega_{p0}$  was  $0.2\Gamma$  [27]. The blockade radius,  $r_B$ , was  $1.9 \mu\text{m}$  according to the formula of  $r_B = (2|C_6|\Gamma/\Omega_c^2)^{1/6}$  [11].  $\Omega_{p0} = 0.2\Gamma$  was the largest input probe Rabi frequency and  $\Omega_c = 1.0\Gamma$  was kept throughout the EIT experiment. Thus, it was considered a weakly-interacting many-body system of Rydberg polaritons, which satisfied the condition of  $(r_B/r_a)^3 \ll 1$ .

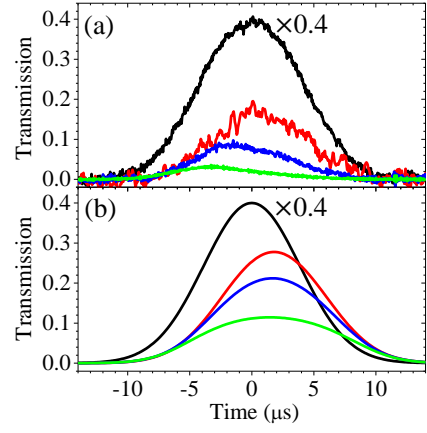


FIG. 2: Experimental observation that the slow light of a Gaussian pulse was distorted and a larger value of  $\Omega_{p0}$  made the distortion more severe. (a) Experimental data of the output pulses versus time are shown by red, blue, and green lines, and their input Rabi frequencies,  $\Omega_{p0}$ , of  $0.05\Gamma$ ,  $0.1\Gamma$ , and  $0.2\Gamma$ , respectively. Since the shape of the three input pulses is very similar, we only plot the one with the  $\Omega_{p0}$  of  $0.1\Gamma$  as shown by the black line, which is scaled down by a factor of 0.4. In the measurements,  $\alpha$  (optical depth) = 70,  $\Omega_c = 1.0\Gamma$ , and  $\gamma_0 = 8.0 \times 10^{-3}\Gamma$ , which were determined experimentally [31]. (b) Theoretical predictions by solving Eqs. (1)-(7) with the above values of  $\Omega_{p0}$ ,  $\alpha$ ,  $\Omega_c$ , and  $\gamma_0$ , and with the coefficient  $A = 0.76\Gamma$  given by Eq. (10).

Using the above experimental conditions, we measured the slow light data as shown in Fig. 2(a). An input probe pulse with a Gaussian  $e^{-1}$  full width of  $11.5 \mu\text{s}$  was used in this measurement. This input pulse was far longer than that used in the determining the OD. Considering the values of OD and  $\Omega_c$ , the delay time  $\tau_d$  was expected to be  $\sim 1.8 \mu\text{s}$  as the result of a short input Gaussian pulse with the  $e^{-1}$  full width of  $0.66 \mu\text{s}$ . However, the peak position of the output pulse with  $\Omega_{p0} = 0.05\Gamma$  of the long Gaussian input probe pulse was nearly the same as the peak position of the input pulse (i.e., the delay time was nearly zero). Furthermore, a stronger input pulse had an output peak position that preceded the input peak position and showed a more distorted shape of the output pulse.

The degree of distortion of the output pulse shape depends on  $\Omega_{p0}$ , or equivalently the Rydberg atom density. One might guess that the DDI effect could explain the distortion, and the experimental data of Fig. 2(a) could be predicted by Eqs. (1)-(7) with the introduction of  $\gamma_{\text{DDI}}$  and  $\delta_{\text{DDI}}$ . To test this hypothesis, we calculated the theoretical predictions as shown in Fig. 2(b) by solving Eqs. (1)-(7), which included the effect of DDI. We used the experimentally-determined values of  $\Omega_{p0}$ ,  $\alpha$ ,  $\Omega_c$ , and  $\gamma_0$  in the calculation. Owing to the DDI effect, i.e., the term of  $\gamma_{\text{DDI}}$  or  $A\rho_{22}$  in Eq. (1), we did observe a lower transmission with a higher value of  $\Omega_{p0}$  in the theoretical prediction. In each case of  $\Omega_{p0}$ , the theoretical prediction gave a very similar delay time ( $\sim 1.8 \mu\text{s}$ ),

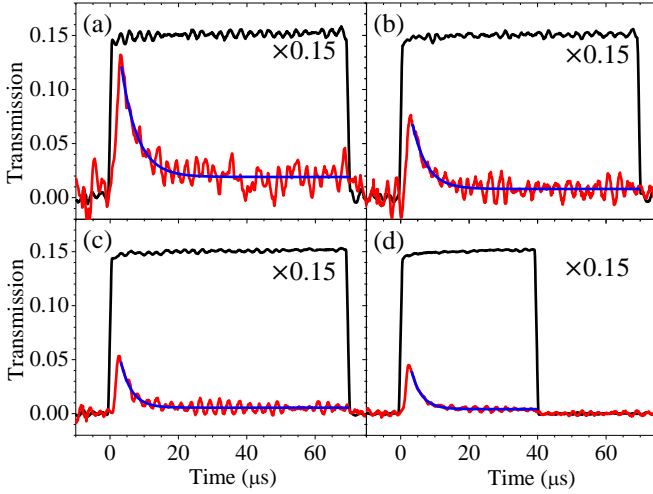


FIG. 3: Experimental observation of the accumulation effect, in which the DDI-induced attenuation increased with time. In each panel, the black line scaled down by a factor of 0.15 is the input pulse, the red line represents the output pulse, and the blue line is the best fit of the tail part of the red line. The best fit is an exponential-decay function. The values of  $\Omega_{p0}$  were (a)  $0.08\Gamma$ , (b)  $0.1\Gamma$ , (c)  $0.15\Gamma$ , and (d)  $0.2\Gamma$ , respectively. In the measurements,  $\alpha$  (optical depth) = 70,  $\Omega_c = 1.0\Gamma$ , and  $\gamma_0 = 1.1 \times 10^{-2}\Gamma$ , which were determined experimentally [31].

which resulted in a higher peak transmission than the experimental value. The theoretical predictions did not agree with the experimental data.

#### D. Phenomenon of the DDI-induced attenuation increasing with time

To further study the phenomenon, we applied the long square probe pulse with the input Rabi frequency  $\Omega_{p0}$  of  $0.08\Gamma$ ,  $0.10\Gamma$ ,  $0.15\Gamma$ , or  $0.2\Gamma$  under the constant presence of the coupling field, as shown in Fig. 3. The experimental parameters of  $\alpha$  (OD) = 70,  $\Omega_c = 1.0\Gamma$ ,  $\Delta = 0$ , and  $\delta = 0$  were kept the same as in the measurements with the Gaussian input, but  $\gamma_0$  was changed to  $1.1 \times 10^{-2}\Gamma$  in the measurement.

Regarding the behavior of the output probe field in Fig. 3, we observed that the transmission decreased (or the attenuation increases) with time, after it reached the peak value in each of the measurements. The peak value of the output probe transmission decreased with  $\Omega_{p0}$ . This was expected from the DDI effect, i.e., the term of  $\gamma_{DDI}$  or  $A\rho_{22}$  in Eq. (1), where  $\rho_{22} \approx \Omega_p^2/\Omega_c^2$ . However, neither the theoretical model nor Eqs. (1)-(7) described in Sec. IIB were not able to explain the phenomenon of the transmission decay or the increasing attenuation over time. We fitted the decayed part of the experimental data with an exponential-decay function, and determined the decay time constant and the steady-state attenuation coefficient. Blue lines shown in Fig. 3 are the best fits.

Based on the best fits in Fig. 3, the decay time con-

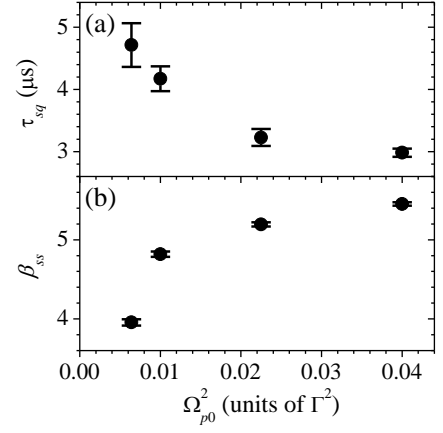


FIG. 4: Experimental observation of a larger  $\Omega_{p0}$  resulting in a faster accumulation of DDI-induced attenuation. (a) Decay time constant,  $\tau_{sq}$ , as a function of  $\Omega_{p0}^2$ . The values of  $\tau_{sq}$  were determined by the best fits shown in Fig. 3. (b) The steady-state attenuation coefficient,  $\beta_{ss}$ , as a function of  $\Omega_{p0}^2$ .  $\beta_{ss} = -\ln(T_{ss})$ , where  $T_{ss}$  is the steady-state transmission. The values of  $T_{ss}$  were determined by the vertical offsets of the blue lines shown in Fig. 3.

stant,  $\tau_{sq}$ , and steady-state attenuation coefficient,  $\beta_{ss}$ , as functions of  $\Omega_{p0}^2$  are shown in Figs. 4(a) and 4(b), respectively. The value of  $\beta_{ss}$  was given by the absolute value of the logarithm of the transmission at the steady state. Figures 4(a) and 4(b) clearly show that a larger value of  $\Omega_{p0}^2$  resulted in a faster decay and a larger steady-state attenuation.

A higher Rydberg polariton density leads to a larger DDI-induced attenuation. Thus, the data in Figs. 3 and 4 inferred that the Rydberg polariton density increased with time. One can guess that some of the Rydberg population in  $|2\rangle$  was transferred to other states (denoted as  $|4\rangle$ ), and that the atoms in  $|4\rangle$  did not interact with the coupling field but were able to have a DDI with the atoms in  $|2\rangle$ . Due to the existence of the DDI,  $|4\rangle$  had to represent some nearby Rydberg states of  $|2\rangle$ . The population in  $|4\rangle$ , which was not driven by the coupling field, should have accumulated. As more population accumulated in  $|4\rangle$ , the DDI-induced attenuation of  $|2\rangle$  became large. Thus, the probe output transmission decreased with time, exhibiting the accumulation phenomenon of the DDI effect.

In Fig. 1(a), we introduce  $|4\rangle$  to represent all possible nearby Rydberg states of  $|2\rangle$ . The spontaneous or collisional decay process could cause the transfer of the population from  $|2\rangle$  to  $|4\rangle$ , because no additional field was applied in the experiment. Since  $|2\rangle$  was driven by the coupling field, it was called the bright Rydberg state. On the other hand,  $|4\rangle$  did not interact with any applied field and was called the dark Rydberg state.

### E. Evidence of dark Rydberg states

To verify the hypothesis based on the dark Rydberg state  $|4\rangle$ , we measured the existing time of the DDI effect, after nearly all the atoms in the bright Rydberg state  $|2\rangle$  had been de-excited. The basic idea of this measurement was as follows. Since the atoms in  $|4\rangle$  did not interact with any applied field, they should decay by themselves and have a decay rate of  $\Gamma_4$ . Furthermore,  $|4\rangle$  represented a number of Rydberg states, so  $\Gamma_4^{-1}$  must be close to the Rydberg-state lifetime. Consequently, after the atoms in  $|2\rangle$  had been removed, the DDI effect should still exist in the system, and gradually decay with the time constant of  $\Gamma_4^{-1}$ . Then, we explored the DDI-induced attenuation as a function of time in the system by employing a very weak Gaussian probe pulse and the coupling field. The probe pulse was weak enough to cause a negligible DDI effect by itself.

The sequence of the input probe field is depicted in the inset of Fig. 5. A 70- $\mu\text{s}$  square probe pulse of  $\Omega_{p0} = 0.1\Gamma$  was first employed. The pulse duration was sufficiently long compared with the lifetime of  $|2\rangle$ , which was approximately 20  $\mu\text{s}$  at room temperature. The OD was 70 and the coupling field of  $\Omega_c = 1.0\Gamma$  was continuously kept on during the measurement. After the square probe pulse was switched off, the coupling field quickly de-excited the remaining population in  $|2\rangle$ . The de-excitation time was estimated to be about 27 ns. We waited for a certain time  $\Delta t$  after the square pulse was turned off, and then applied a weak Gaussian probe pulse to measure the DDI-induced attenuation,  $\beta_G$ , as a function of  $\Delta t$ . The value of  $\beta_G$  was equal to the absolute value of the logarithm of the peak transmission of the output Gaussian pulse. The input Gaussian pulse had the peak  $\Omega_{p0}$  of  $0.05\Gamma$  and the  $e^{-1}$  full width of 10  $\mu\text{s}$ . Compared with the 70- $\mu\text{s}$  square probe pulse, the weaker and much shorter Gaussian probe pulse induced a negligible DDI effect.

We observed the exponential-decay behavior of  $\beta_G$  versus  $\Delta t$  as shown in Fig. 5 in which the circles are the experimental data and the black line is the best fit of an exponential-decay function. The decay time constant of the best fit was 31  $\mu\text{s}$ , which is about the lifetime of a Rydberg state with a principal quantum number between 32 and 38. The atoms in  $|2\rangle$  were quickly de-excited by the coupling field, after the square probe pulse was switched off. If the atoms in the dark Rydberg state  $|4\rangle$  could not exist in the system, the value of  $\beta_G$  would quickly drop to its steady-state value due to the absence of the atoms in the bright Rydberg state  $|2\rangle$ . The slow decay of  $\beta_G$  demonstrated the existence of the atoms in  $|4\rangle$ , which did not interact with the coupling field, but gave the DDI effect and decayed slowly.

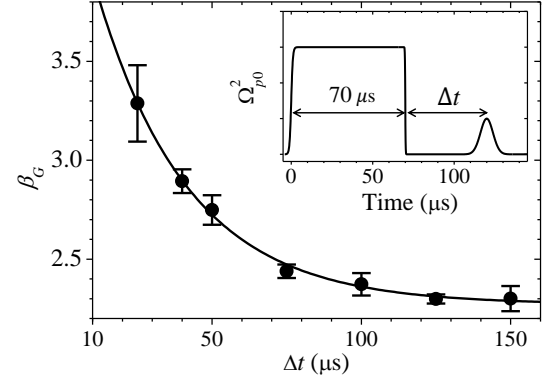


FIG. 5: Experimental observation of the lifetime of the dark Rydberg states by the measurement of DDI-induced attenuation  $\beta_G$  as a function of  $\Delta t$ . Inset: the time sequence of the measurement. The coupling field was continuously on during the measurement. Circles are the experimental data and the black line is the best fit of an exponential-decay function. The decay time constant of the best fit was 31  $\mu\text{s}$ , which is similar to the lifetimes of dark Rydberg states with the principal quantum number,  $n$ , of around 32.

## III. THEORY OF THE ACCUMULATION EFFECT AND EXPERIMENTAL VERIFICATION

### A. Theoretical model with the accumulation effect

In the previous section, we discussed the necessity of the consideration of dark Rydberg states in the system. To simulate the accumulative DDI effect observed in the experiment, we improved the theoretical model described in Subsec. IIB by including the dark Rydberg state  $|4\rangle$  and the decay process from  $|2\rangle$  to  $|4\rangle$ . The DDI effect between one atom in  $|2\rangle$  and one atom in  $|4\rangle$  was also taken into account. Thus, the OBEs can be given by:

$$\begin{aligned} \frac{\partial}{\partial t} \rho_{21} &= \frac{i}{2} \Omega_c \rho_{31} + i(A\rho_{22} + B'\rho_{44} + \delta)\rho_{21} \\ &\quad - \left( A\rho_{22} + B\rho_{44} + \gamma_0 + \frac{\Gamma_{24}}{2} \right) \rho_{21}, \end{aligned} \quad (13)$$

$$\begin{aligned} \frac{\partial}{\partial t} \rho_{31} &= \frac{i}{2} \Omega_p (\rho_{11} - \rho_{33}) + \frac{i}{2} \Omega_c \rho_{21} + i\Delta_p \rho_{31} \\ &\quad - \frac{\Gamma}{2} \rho_{31}, \end{aligned} \quad (14)$$

$$\begin{aligned} \frac{\partial}{\partial t} \rho_{32} &= \frac{i}{2} \Omega_p \rho_{21}^* + \frac{i}{2} \Omega_c (\rho_{22} - \rho_{33}) \\ &\quad - i\Delta_c \rho_{32} - \frac{\Gamma}{2} \rho_{32}, \end{aligned} \quad (15)$$

$$\frac{\partial}{\partial t} \rho_{22} = \frac{i}{2} \Omega_c \rho_{32} - \frac{i}{2} \Omega_c \rho_{32}^* - \Gamma_{24} \rho_{22}, \quad (16)$$

$$\begin{aligned} \frac{\partial}{\partial t} \rho_{33} &= -\frac{i}{2} \Omega_p^* \rho_{31} + \frac{i}{2} \Omega_p \rho_{31}^* - \frac{i}{2} \Omega_c \rho_{32} \\ &\quad + \frac{i}{2} \Omega_c \rho_{32}^* - \Gamma \rho_{33}, \end{aligned} \quad (17)$$

$$\frac{\partial}{\partial t} \rho_{44} = \Gamma_{24} \rho_{22} - \Gamma_4 \rho_{44}, \quad (18)$$



$$\frac{\partial}{\partial t}\rho_{11} = \frac{i}{2}\Omega_p^*\rho_{31} - \frac{i}{2}\Omega_p\rho_{31}^* + \Gamma\rho_{33}, \quad (19)$$

where the coefficient  $A$  represents the DDI-induced decoherence rate or frequency shift per unit  $\rho_{22}$  with a value given by Eq. (10), the coefficient  $B$  (or  $B'$ ) is similar to the coefficient  $A$  and represents the DDI-induced decoherence rate (or frequency shift) per unit  $\rho_{44}$ ,  $\Gamma_{24}$  is the decay rate from  $|2\rangle$  to  $|4\rangle$ , and  $\Gamma_4$  is the decay rate of  $|4\rangle$ .

The terms  $A\rho_{22} + B'\rho_{44}$  and  $A\rho_{22} + B\rho_{44}$  in Eq. (13) represent  $\delta_{\text{DDI}}$  and  $\gamma_{\text{DDI}}$ , respectively. The values of  $\gamma_{\text{DDI}}$  and  $\delta_{\text{DDI}}$  varied with space and time due to the populations of  $\rho_{22}(z, t)$  and  $\rho_{44}(z, t)$  during the propagation of the probe light. The decay rate  $\Gamma_{24}$  was parametrized as:

$$\Gamma_{24} \equiv C(\rho_{22} + \rho_{44}) + D, \quad (20)$$

where the coefficient  $C$  is the two-body decay rate per unit  $\rho_{22}$  or  $\rho_{44}$ , and the coefficient  $D$  is the one-body decay rate. The atomic density,  $n_a$ , of the system is a part of the coefficient  $C$ . In reality, the values of  $C(\rho_{22} + \rho_{44})$  and  $D$  can be the collisional decay rate between two Rydberg atoms and the spontaneous decay rate, respectively, and the two decay processes transfer the population from  $|2\rangle$  to  $|4\rangle$ .

In Eq. (15), the DDI effect, i.e.,  $\gamma_{\text{DDI}}$  and  $\delta_{\text{DDI}}$ , and the decay rates, i.e.,  $\Gamma_{24}$ , and  $\Gamma_2$ , were ignored due to the experimental condition of  $A\rho_{22}, B\rho_{44}, \Gamma_{24}, \Gamma_2 \ll \Gamma$ . Please note that the frequency shift induced by the population in each of the dark Rydberg states might be positive or negative, and thus the net frequency shift resulted in  $|B'| \leq B$ . Furthermore, the term of  $i(A\rho_{22} + B'\rho_{44} + \delta)\rho_{21}$  in Eq. (13) played a negligible role in the output probe transmission, since  $\delta = 0$  and  $4|A\rho_{22} + B\rho_{44}|^2\Gamma^2 \ll \Omega_c^4$  in all the cases of this work.

The value of  $A$  given by Eq. (10) was derived from Ref. [27] and experimentally verified in Ref. [28]. We first measured the coefficients  $C$  and  $D$  as described in Subsec. III C. Using the known values of  $A$ ,  $C$ , and  $D$ , we then determined  $B$  using the experimental data of Fig. 3 as illustrated in Subsec. III D. Finally, we compared the experimental data of the slow light shown in Fig. 2 with the theoretical predictions calculated using the experimentally determined values of  $A$ ,  $B$ ,  $C$ , and  $D$  in Subsec. III D. The comparison was used to test the validity of the theoretical model introduced here.

### B. Experimental setup for measuring the decay rate of the bright Rydberg state

We designed an experiment to determine the coefficients  $C$  and  $D$  in Eq. (20). The decay rate,  $\Gamma_{24}$ , of the atoms in  $|2\rangle$  was measured against the atomic density of  $|2\rangle$ ,  $n_R$ . The procedure of the measurement of  $\Gamma_{24}$  was as follows. We first prepared a given number of atoms in the ground state  $|1\rangle$  and excited them to  $|2\rangle$  with a two-photon transition (TPT) pulse. The TPT had a large one-photon detuning as shown in Fig. 6(a). After the

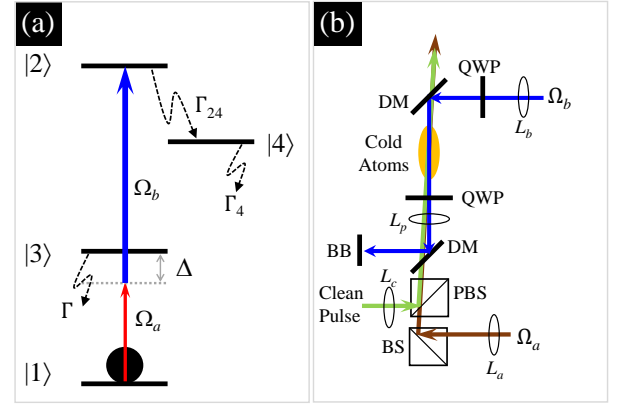


FIG. 6: (a) Scheme of the two-photon transition, which moved the population from  $|1\rangle$  to  $|2\rangle$ . The energy levels here were the same as those in Fig. 1. Please note that  $|1\rangle \rightarrow |3\rangle$  is a cycling transition and, thus, population of any undesired transition to  $|3\rangle$  quickly decayed back only to  $|1\rangle$ .  $\Omega_a$  and  $\Omega_b$  denote the Rabi frequencies of the two square pulses of the laser fields. We kept the frequencies of  $\Omega_a$  and  $\Omega_b$  to the two-photon resonance, and applied a one-photon detuning ( $\Delta$ ) of  $4\Gamma$  to  $\Omega_b$  or that of  $-4\Gamma$  to  $\Omega_a$ .  $\Gamma$  and  $\Gamma_4$  are the spontaneous decay rates of  $|3\rangle$  and  $|4\rangle$ , respectively.  $\Gamma_{24}$  is the decay rate from  $|2\rangle$  to  $|4\rangle$ . (b) Optical paths of  $\Omega_a$ ,  $\Omega_b$ , and a clean pulse in the experiment.  $\Omega_b$  was the same as that of the coupling field, but had a different frequency. The clean pulse was employed to wipe out the population in  $|1\rangle$ .

TPT pulse, no light field was applied, and the atoms in  $|2\rangle$  decayed. Then, we waited for a certain time  $\Delta t$ , and also depleted the residual atoms in  $|1\rangle$ . At the end of  $\Delta t$ , the remaining atoms in  $|2\rangle$  were brought back to  $|1\rangle$  with another TPT pulse. Finally, after the second TPT pulse we determined the number of the returned atoms in  $|1\rangle$  or, equivalently, measured the absorption coefficient,  $\Delta\beta$ , of the weak probe field. The result of  $\Delta\beta$  was proportional to the remaining atoms in  $|2\rangle$  after the given  $\Delta t$ . By varying  $\Delta t$  and measuring  $\Delta\beta$ , we obtained the data points of  $\Delta\beta$  as a function of  $\Delta t$ , and fitted the data with an exponential function. The best fit gave the value of  $\Gamma_{24}$ .

We employed the TPT scheme rather than the EIT scheme to place the population in  $|2\rangle$ , because the TPT scheme is able to move a large portion of the atoms in  $|1\rangle$  to  $|2\rangle$ . In the measurement of  $\Gamma_{24}$ , we added the pulses of  $\Omega_a$  and  $\Omega_b$ , which formed the TPT pulse, and the clean pulse as shown in Fig. 6(b). The coupling field ( $\Omega_c$ ) in the EIT experiment was utilized as  $\Omega_b$ , but we changed its frequency to set the one-photon detuning,  $\Delta$ , to  $4.0\Gamma$  for the TPT as depicted in Fig. 6(a). The frequency of  $\Omega_a$  was tuned such that the TPT satisfied the two-photon resonance. A weak and resonant probe pulse, denoted as  $\Omega_{p'}$ , was used in the measurement. The pulse of  $\Omega_{p'}$  had the same optical path as the field of  $\Omega_p$  shown in Fig. 1(b). The absorption coefficient of  $\Omega_{p'}$  indicated the number of atoms in  $|1\rangle$ .

The polarization, propagation direction, and beam size

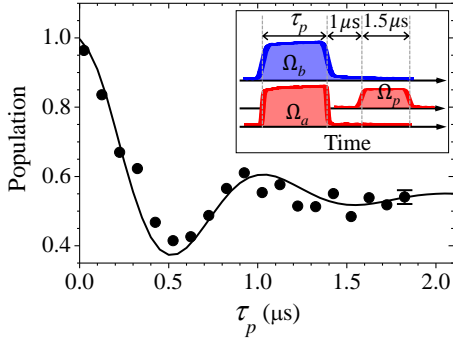


FIG. 7: Experimental demonstration of the two-photon transition (TPT) shown in Fig. 6(a). In the main figure, we plot the remaining population in state  $|1\rangle$  after the TPT pulse as a function of the TPT pulse width,  $\tau_p$ . In the inset, we show the timing sequence of the pulses of  $\Omega_a$  and  $\Omega_b$  (to drive the TPT) and  $\Omega_{p'}$  (to measure the population in  $|1\rangle$ ), as well as their pulse shapes. We set  $\Delta = 4.0\Gamma$ ,  $\alpha$  (optical depth) = 0.5,  $\Omega_a = \Omega_b = 1.2\Gamma$ , and  $\Omega_{p'0} = 0.08\Gamma$  in the measurement. Circles are the experimental data, which have similar error bars. Only the last data point shows the error bar, which represents the typical value. The black line is the theoretical prediction of a simple three-level cascade system under the two-photon resonance. The prediction was calculated with the decoherence rate of  $6.5 \times 10^{-2}\Gamma$ , and the above values of  $\Delta$ ,  $\Omega_a$ , and  $\Omega_b$ .

of  $\Omega_b$  (or  $\Omega_{p'}$ ) were the same as those of  $\Omega_c$  (or  $\Omega_p$ ) in the EIT experiment. The field of  $\Omega_a$  was generated by a diode laser, which was injection-locked by the same laser that generated the field of  $\Omega_p$  in the EIT experiment. Hence, the two-photon frequency of  $\Omega_a$  and  $\Omega_b$  was stable. The pulse of  $\Omega_a$  was sent to the atom cloud by a PMF after passing through an AOM. The clean pulse was used to remove the population in  $|1\rangle$ . After passing through the AOM, the clean pulse had a frequency that was resonant to the transition of  $|5S_{1/2}, F=2\rangle \rightarrow |5P_{3/2}, F=2\rangle$ . The polarization of  $\Omega_a$  and the clean pulse were  $\sigma_+$  and  $\sigma_-$ , respectively. There was a separation angle of  $0.36^\circ$  (or  $0.40^\circ$ ) between the propagation directions of  $\Omega_a$  (or the clean pulse) and  $\Omega_b$ . Lens  $L_a$  (or  $L_c$ ) was used together with  $L_p$  to make  $\Omega_a$  (or the clean pulse) a collimated beam with the  $e^{-1}$  full width of 3.6 mm (or 4.5 mm). The two beam sizes of  $\Omega_a$  and the clean pulse were sufficiently large to cover the entire atom cloud.

To study the efficiency of the TPT pulse, i.e., the simultaneous pulses of  $\Omega_a$  and  $\Omega_b$ , we varied the TPT pulse duration,  $\tau_p$ , and measured the population or atom number right after the TPT pulse as shown in Fig. 7. The population in  $|1\rangle$  was determined by the absorption coefficient of  $\Omega_{p'}$ . The timing sequence of  $\Omega_a$ ,  $\Omega_b$ ,  $\Omega_{p'}$ , and their pulse shapes are depicted in the inset. In the main plot, the circles are the experimental data, and the line is the theoretical prediction of a simple three-level cascade system under the two-photon resonance, i.e., Eqs. (1)-(6) are utilized with  $\delta = 0$ ,  $\delta_{\text{DDI}} = 0$ ,  $\gamma_{\text{DDI}} = 0$ ,  $\Omega_p \rightarrow \Omega_a$ , and  $\Omega_c \rightarrow \Omega_b$ . To calculate the prediction, we set  $\Delta$ ,

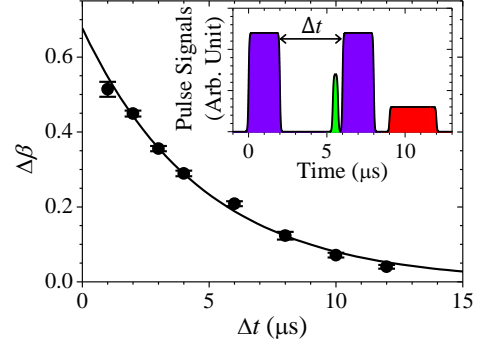


FIG. 8: Determination of the decay rate of the bright Rydberg state  $|2\rangle$ . The inset shows the time sequence of the measurement. The purple, green, and red areas represent the two-photon transition (TPT) pulses, the clean pulse, and the probe pulse, respectively. In the main plot, circles are the representative data of the difference between the absorption coefficients with and without the second TPT pulse,  $\Delta\beta$ , as a function of  $\Delta t$ . The black line is the best fit of an exponential-decay function, which determined the decay rate. In the measurement of these data points,  $n_R = 0.002 \mu\text{m}^{-3}$ , and the values of  $\Delta$ ,  $\Omega_a$ ,  $\Omega_b$ , and  $\Omega_{p'0}$  were the same as those in shown Fig. 7.

$\Omega_a$ , and  $\Omega_b$  to the experimental values, and adjusted  $\gamma_0$  to match the experimental data. The fair agreement between the data and the prediction verified the effect of the TPT pulse on the population. According to the study shown in Fig. 7, we decided to use a  $1.8 \mu\text{s}$  TPT pulse with  $\Delta = 4.0\Gamma$  and  $\Omega_a = \Omega_b = 1.2\Gamma$  in the measurement of  $\Gamma_{24}$  because the transition probability after  $\tau_p = 1.8 \mu\text{s}$  was insensitive to the pulse width. Please note that the reduced population in  $|1\rangle$  was used to determine the population in  $|2\rangle$ , but during the TPT pulse the excitation to the intermediate state  $|3\rangle$  was not negligible. Nevertheless, since the population in  $|3\rangle$  decayed only to  $|1\rangle$  in a rather short time right after the TPT pulse, the excitation of the population to  $|3\rangle$  did not affect the determination of the population in  $|2\rangle$ .

### C. Determination of the decay rate from bright to dark Rydberg states

To obtain the decay rate,  $\Gamma_{24}$ , of the atoms in  $|2\rangle$  as a function of the density,  $n_R$ , of the atoms in  $|2\rangle$ , we performed the measurement described in the first paragraph of Subsec. III B. The time sequence of the measurement is depicted in the inset of Fig. 8. We kept the time difference between the peak of the clean pulse and the rising edge of the second TPT pulse to about 400 ns, and that between the falling edge of the second TPT pulse and the rising edge of the probe pulse to about  $1 \mu\text{s}$ . Each of the two TPT pulses had a duration of  $1.8 \mu\text{s}$ . The TPT pulse was able to move a fixed fraction (about half) of the atoms from the initial state to the final state, i.e.,  $|1\rangle \rightarrow |2\rangle$  or  $|2\rangle \rightarrow |1\rangle$ . The residual atoms either were



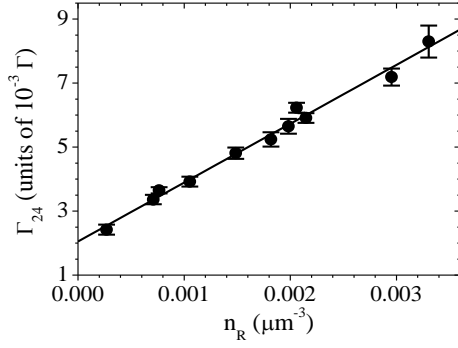


FIG. 9: The decay rate  $\Gamma_{24}$  as a function of the density,  $n_R$ , of the atoms in  $|2\rangle$ . Based on Eq. (21), the value of  $n_R$  was determined by  $\Delta\alpha$ , which was the difference of the values of OD between before and after the first TPT. Circles are the experimental data. Each data point was determined by the result of a series of measurements similar to those in Fig. 8. The black line is the best fit of a straight line.

removed from the system or did not affect the measurement of the decay rate. We varied  $\Delta t$  and measured the absorption coefficient,  $\Delta\beta$ , of the weak probe pulse,  $\Omega_{p'}$ . The representative data of the difference between the values of  $\Delta\beta$  with and without the second TPT pulse as a function of  $\Delta t$  are plotted in Fig. 8. Since the atoms in  $|1\rangle$  right before the second TPT were all depleted by the clean pulse,  $\Delta\beta$  corresponded to the remaining atoms in  $|2\rangle$  after a decay time of  $\Delta t$ .

The data points in Fig. 8 were all taken at  $\Delta\alpha = 2.9$ , where  $\Delta\alpha$  is defined as the difference of the values of OD before and after the first TPT pulse. The two values of OD were about 5.2 and 2.3 in this case. We were able to estimate the density of the atoms in  $|2\rangle$  after the first TPT pulse from  $\Delta\alpha$  using the following relation:

$$\Delta\alpha = \sigma_0 n_1 L = \sigma_0 n_R L, \quad (21)$$

where  $\sigma_0$  is the absorption cross section of the resonant probe transition from  $|5S_{1/2}, F=2, m_F=2\rangle$  to  $|5P_{3/2}, F=3, m_F=3\rangle$ , and  $n_1$  is the density of the atoms in  $|1\rangle$  that were moved to  $|2\rangle$  by the first TPT pulse. Consequently,  $n_1$  was equal to the initial Rydberg-atom density  $n_R$ , which participated in the decay process of  $|2\rangle$ . As shown in Fig. 8, we fitted the experimental data taken at a given  $n_R$  with an exponential-decay function. The decay time constant of the best fit gave the value of  $\Gamma_{24}$  of the given  $n_R$ .

The circles in Fig. 9 are the experimental data of  $\Gamma_{24}$  as a function of  $n_R$ . Each circle represents the result of a series of measurements similar to those shown in Fig. 8. We fitted the circles in Fig. 9 with the fitting function of a straight line. The interception of the best fit determined the coefficient  $D$  defined in Eq. (20), which was  $2.0 \times 10^{-3} \Gamma$ . The determined value of  $D$  was comparable to the spontaneous decay rate of  $32D_{5/2}$  at room temperature, which is  $1.3 \times 10^{-3} \Gamma$  [33, 34]. Furthermore, the slope,  $k$ , of the best fit determined the coefficient  $C$  defined in Eq. (20) in the following way: Since  $k n_R = C \rho_{22}$

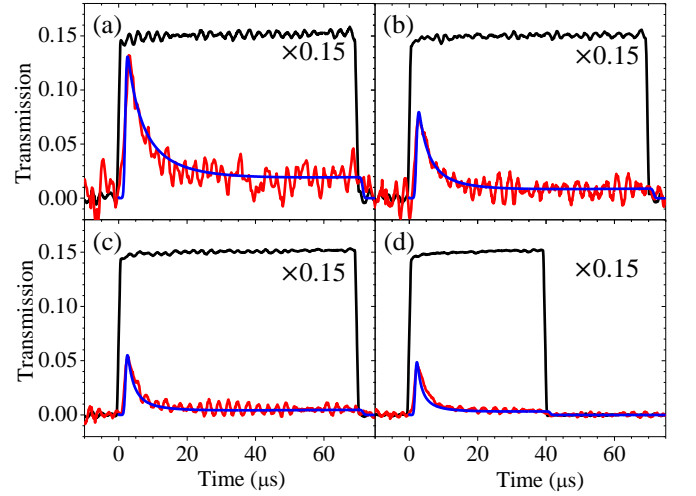


FIG. 10: Comparison between the experimental data of the long square probe pulses and the theoretical predictions. Black lines represent the input probe pulses and are scaled down by a factor of 0.15. Red lines represent the output probe pulses under the constant presence of the coupling field. The experimental data are the same as those shown in Fig. 3, where the input Rabi frequencies  $\Omega_{p0}$  are (a)  $0.08\Gamma$ , (b)  $0.1\Gamma$ , (c)  $0.15\Gamma$ , and (d)  $0.2\Gamma$ . Blue lines are the predictions calculated using Eqs. (7) and (13)-(20). In the calculation, we set  $\alpha$  (optical depth) = 70,  $\Omega_c = 1.0\Gamma$ , and  $\gamma_0 = 1.1 \times 10^{-2} \Gamma$ , which were determined experimentally, the coefficients  $C = 9.1 \times 10^{-2} \Gamma$  and  $D = 1.3 \times 10^{-3} \Gamma$ , which were deduced from the result of Fig. 9, and  $A = 0.76\Gamma$  given by Eq. (10).  $B$  was adjusted to make the predictions fit the data and its optimum value is  $7.7 \Gamma$ .

and  $n_R = \rho_{22} n_a = \rho_{22} \alpha / (\sigma_0 L)$ , the coefficient  $C$  is given by:

$$C = k\alpha / (\sigma_0 L), \quad (22)$$

where  $\alpha$  is the OD used in the EIT experiment. During the measurements of the data shown in Figs. 2(a) and 3(a)-3(d), the optical depth ( $\alpha$ ) was 70, we used the above equation to estimate that the value of  $C$  was  $9.1 \times 10^{-2} \Gamma$  at  $\alpha = 70$ . Possible processes of the population transfer from the bright to dark Rydberg states are discussed in Sec. IV.

#### D. Comparison between theoretical predictions and experimental results

After determining the values of  $C$  and  $D$  in the decay rate  $\Gamma_{24}$  used in Eqs. (13), (16), and (18), we next utilized the experimental data of Fig. 3 to determine the value of coefficient  $B$  used in Eq. (13). Since the measured value of  $\Gamma_{24}$  was the total decay rate of  $|2\rangle$  but not merely the decay rate from  $|2\rangle$  to  $|4\rangle$ , the determined value of  $B$  might account for the discrepancy. Figure 10 shows the comparison between the experimental data of the long square probe pulses shown in Figs. 3(a)-3(d) and the theoretical predictions calculated with the modified model

described in Sec. III A. In the calculation, we used the experimentally determined values of the optical depth, the coupling Rabi frequency, and intrinsic decoherence rate  $\gamma_0$  in the system [31]. We set  $A$  (the DDI-induced decoherence rate per unit  $\rho_{22}$ ) to the value given by Eq. (10), and used the values of  $C$  and  $D$  derived from the result of Fig. 9. The only adjustable parameter in the calculation of the predictions was  $B$  (the DDI-induced decoherence rate per unit  $\rho_{44}$ ). Note that we set  $B' = B$  in the term of  $i(A\rho_{22} + B'\rho_{44} + \delta)\rho_{21}$  in Eq. (13), but this term played a negligible role in the calculation result of the output probe transmission. A good agreement between the theoretical predictions and experimental data was obtained at the coefficient  $B = 7.7 \Gamma$ .

A single optimum value of  $B$  was able to explain all the experimental data taken at different input probe Rabi frequencies. This demonstrated the theoretical model presented by Eqs. (13)-(20) was qualitatively valid. Furthermore, we compared the experimental data of the Gaussian input probe pulses as shown in Fig. 2 with the theoretical predictions. The values of the parameters used in the calculation of the predictions were the same as those in Fig. 10 except for the value of  $\gamma_0$ , which had a day-to-day fluctuation of  $1.5 \times 10^{-3} \Gamma$ . Figures 11(a)-11(c) show that the experimental data were all in good agreement with the theoretical predictions, manifesting that the theoretical model was also quantitatively successful.

#### IV. DISCUSSION

Experimental observations of population transfer from one Rydberg state to another, i.e., from a bright Rydberg state to the dark Rydberg state, have been reported in several articles [36–40]. The underlying mechanisms of such transfers can be transitions driven by a microwave field [36], the spontaneous decay induced by black-body radiation and vacuum fluctuations [37–39], and the DDI-induced antiblockade excitation and state-exchange collision assisted by radiation trapping [40]. The mechanism investigated in this study was DDI-induced state-exchange collisions without radiation trapping. We discuss these articles and compare their results and experimental conditions with our observations and experimental condition in the following paragraphs.

The authors in Ref. [36] measured the linewidth of the transition from  $|45D_{5/2}\rangle$  to  $|46D_{5/2}\rangle$ , while the entire Rydberg population was initially prepared in  $|45D_{5/2}\rangle$ . As they moved half of the Rydberg population to  $|46P_{3/2}\rangle$  by applying a microwave before the linewidth measurement, the measured linewidth was broadened. The authors explained that the DDI between a  $|45D_{5/2}\rangle$  atom and a  $|46P_{3/2}\rangle$  atom was stronger than that between two  $|45D_{5/2}\rangle$  atoms, resulting in the linewidth broadening. The population transfer from the bright ( $|45D_{5/2}\rangle$ ) to dark ( $|46P_{3/2}\rangle$ ) Rydberg state was intentionally driven by a microwave field, and no accumulative DDI effect was reported in Ref. [36]. Since we did not apply any ad-

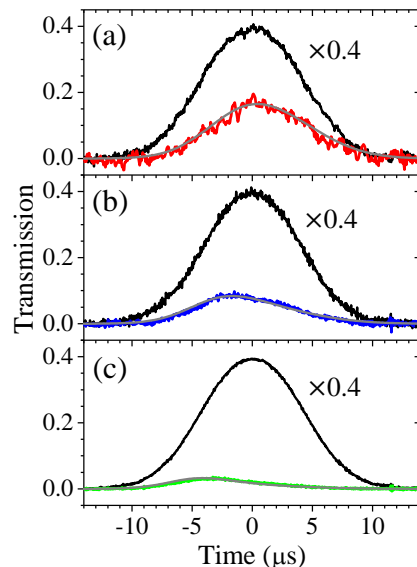


FIG. 11: Comparison between the experimental data of the Gaussian input probe pulses and the theoretical predictions. Black lines represent the input probe pulses and are scaled down by a factor of 0.4. Red, blue, and green lines represent the output probe pulses under the constant presence of the coupling field. The experimental data are the same as those shown in Fig. 2, where the input Rabi frequencies  $\Omega_{p0}$  are (a)  $0.05\Gamma$ , (b)  $0.1\Gamma$ , and (c)  $0.2\Gamma$ . Gray lines are the theoretical predictions calculated with Eqs. (7) and (13)-(20). All the parameters used in the calculation here are the same as those used in Fig. 10, except for  $\gamma_0 = 9.0 \times 10^{-3} \Gamma$ .

ditional field to move the population from the bright to dark Rydberg states, the physical mechanism in this reference is unable to explain the accumulative DDI effect observed in our study.

On the other hand, the population in the dark Rydberg state could be produced via the spontaneous decay from the bright Rydberg state induced by the black-body radiation and vacuum fluctuation. In Ref. [37], the authors measured the spectrum of the two-photon transition from a ground state to the Rydberg state  $|18S_{1/2}\rangle$  with the  $^{87}\text{Rb}$  atoms trapped in a 3D optical lattice. They observed that the measured linewidth was about two orders of magnitude larger than the expected linewidth due to the DDI between two  $|18S_{1/2}\rangle$  atoms. Such a large linewidth was explained by the DDI between an atom in  $|18S_{1/2}\rangle$  and another in a nearby Rydberg state,  $|17P\rangle$  or  $|18P\rangle$ . The existence of the population in  $|17P\rangle$  and  $|18P\rangle$  due to the spontaneous decay from  $|18S_{1/2}\rangle$  was further verified by Ref. [38]. In Ref. [39], the authors reported a similar phenomenon with the bright Rydberg state of  $|28D_{5/2}\rangle$  and the dark Rydberg states of  $|26F_{7/2}\rangle$ ,  $|27F_{7/2}\rangle$ ,  $|29P_{3/2}\rangle$ , and  $|30P_{3/2}\rangle$ . Nevertheless, the spontaneous decay was an one-body process and did not depend on the Rydberg-atom density. As shown in Fig. 9, the observed decay rate linearly depended on the atomic density of the bright Rydberg state. Furthermore,

it was also larger than the spontaneous decay rate of  $|32D_{5/2}\rangle$  used in our experiment, which was  $2\pi \times 7.9$  kHz or  $1.3 \times 10^{-3}$   $\Gamma$ . Thus, the decay from the bright to dark Rydberg states observed in this study is unable to be explained by the spontaneous decay.

Population transfer from the bright to dark Rydberg states can also be induced by the direct antiblockade excitation [41, 42] and state-changing Rydberg collisions [43–46]. In Ref. [40], the authors drove the Rydberg-EIT transition from a ground state to  $|111S_{1/2}\rangle$  (the bright Rydberg state) and detected the ions coming from a number of dark Rydberg states (nearby states other than  $|111S_{1/2}\rangle$ ) after an ionization pulse. Compared with the experiment in our work, the experiment in the reference was carried out under a high atomic density of  $5 \times 10^{12}$   $\text{cm}^{-3}$  and in the strong-interaction regime of  $(r_B/r_a)^3 > 1$ . Under such an atomic density, the authors in Ref. [40] explained that the effect of radiation trapping was prominent, producing more atoms in the bright Rydberg state. The atoms produced by the radiation trapping had all possible angular momentum angles. Then, the strong-interaction regime enabled the DDI-induced antiblockade excitation and state-changing collisions to generate dark Rydberg atoms from the bright Rydberg atoms. These dark Rydberg atoms produced ions after an ionization pulse, while the ions were clearly not able to come from the bright Rydberg state  $|111S_{1/2}\rangle$ . The dark Rydberg atom also resulted in the unexpected reduction of the output probe photon number. The authors stated that the reduction is unable to be explained by the prediction of the blockade effect with only the bright Rydberg state but no dark Rydberg states.

In our experiment, the population transfer from the bright to dark Rydberg states should be caused by the DDI-induced state-changing collisions. This experiment was carried out under a much lower atomic density of  $4 \times 10^{10}$   $\text{cm}^{-3}$  and in the weak-interaction regime, i.e.,  $(r_B/r_a)^3 < 0.06$ , as compared with the experiment in Ref. [40]. Under such an atomic density, the radiation trapping effect was not significant. Nevertheless, according to the input power and propagation delay time of the probe pulse, there were many bright Rydberg atoms in the system. In the weak-interaction regime, it took these bright Rydberg atoms a considerable time to generate dark Rydberg atoms via the state-changing collisions. Thus, the transmission of the output probe light in our experiment required a longer time constant to reach the steady state than that in Ref. [40]. Furthermore, the lifetime of the dark Rydberg atoms determined in Fig. 5 was about 31  $\mu\text{s}$ , which was very long compared with that determined in Ref. [40]. Consequently, a sufficient amount of the dark Rydberg atoms were accumulated to strongly influence the transmission of the output probe light even in the weak-interaction regime.

## V. CONCLUSION

In this work, we systematically studied the transmission of a probe field propagating through a Rydberg EIT system, in which the DDI strength was in the weak interaction regime. As shown in Fig. 2(a), we observed the distorted output of a long Gaussian input probe pulse. The distortion was enhanced with a stronger input probe Rabi frequency,  $\Omega_{p0}$ . Such a phenomenon was unable to be predicted by the theoretical model, which only considered the DDI between the bright Rydberg atoms as demonstrated by Fig. 2(b). According to the further experimental data shown in Figs. 3-5, there existed atoms in the dark Rydberg states which were not driven by the coupling field. The dark Rydberg atoms came from the decay of the bright Rydberg atoms. Without the interaction with the coupling field, the dark Rydberg atoms accumulated. The dark and bright Rydberg atoms had the DDI effect with each other. As the number of dark Rydberg atoms increased due to the accumulation, the DDI effect on the bright Rydberg atoms became larger. Equivalently, in the EIT system the DDI-induced attenuation of the probe field increased with time.

To simulate the accumulation phenomenon of the DDI effect, we introduced the coefficients  $A, B, C$ , and  $D$  to the modified OBEs.  $A$  and  $B$  described the DDI effect between the two bright Rydberg atoms and that between one bright and one dark Rydberg atoms, respectively.  $C$  and  $D$  were associated with the two-body (state-changing collisional) decay and one-body (spontaneous) decay processes from the bright to dark Rydberg states, respectively. We measured the decay rate of the bright Rydberg atoms, and the representative data of the measurement are demonstrated in Fig. 8. The values of  $C$  and  $D$  were determined by the decay rate of the bright Rydberg atoms as a function of their density as shown in Fig. 9. Furthermore, the value of  $A$  was experimentally determined in Ref. [28] and that of  $B$  by the data shown in Fig. 10. Finally, the theoretical predictions, which were calculated using the determined values of  $A, B, C$ , and  $D$ , were in good agreements with the experiment data of slow light as shown in Fig. 11. In conclusion, this study provided a better understanding of the DDI effect under a long interaction time [47–49], and pointed out a possible issue in the realization of the Bose-Einstein condensation of Rydberg polaritons [28, 50].

## Acknowledgements

This work was supported by Grant Nos. 109-2639-M-007-001-ASP and 110-2639-M-007-001-ASP of the Ministry of Science and Technology, Taiwan.

---

[1] M. D. Lukin, M. Fleischhauer, R. Cote, L. M. Duan, D. Jaksch, J. I. Cirac, and P. Zoller, Dipole Blockade and

- Ensembles, *Phys. Rev. Lett.* **87**, 037901 (2001).
- [2] D. Comparat, and P. Pillet, Dipole blockade in a cold Rydberg atomic sample, *J. Opt. Soc. Am. B* **27**, A208 (2010).
  - [3] M. Saffman, T. G. Walker, and K. Mølmer, Quantum information with Rydberg atoms, *Rev. Mod. Phys.* **82**, 2313 (2010).
  - [4] T. Baluktian, B. Huber, R. Löw, and T. Pfau, Evidence for Strong van der Waals Type Rydberg-Rydberg Interaction in a Thermal Vapor, *Phys. Rev. Lett.* **110**, 123001 (2013).
  - [5] D. Tiarks, S. Schmidt-Eberle, T. Stolz, G. Rempe, and S. Dürr, A photon-photon quantum gate based on Rydberg interactions, *Nature Phys.* **15**, 124 (2019).
  - [6] H. Gorniaczyk, C. Tresp, J. Schmidt, H. Fedder, and S. Hofferberth, Single-Photon Transistor Mediated by Inter-state Rydberg Interactions, *Phys. Rev. Lett.* **113**, 053601 (2014).
  - [7] D. Tiarks, S. Baur, K. Schneider, S. Dürr, and G. Rempe, Single-Photon Transistor Using a Förster Resonance, *Phys. Rev. Lett.* **113**, 053602 (2014).
  - [8] S. Baur, D. Tiarks, G. Rempe, and S. Dürr, Single-Photon Switch Based on Rydberg Blockade, *Phys. Rev. Lett.* **112**, 073901 (2014).
  - [9] J. D. Pritchard, D. Maxwell, A. Gauguier, K. J. Weatherill, M. P. A. Jones, and C. S. Adams, Cooperative Atom-Light Interaction in a Blockaded Rydberg Ensemble, *Phys. Rev. Lett.* **105**, 193603 (2010).
  - [10] D. Petrosyan, J. Otterbach, and M. Fleischhauer, Electromagnetically Induced Transparency with Rydberg Atoms, *Phys. Rev. Lett.* **107**, 213601 (2011).
  - [11] T. Peyronel, O. Firstenberg, Q.-Y. Liang, S. Hofferberth, A. V. Gorshkov, T. Pohl, M. D. Lukin, and V. Vuletić, Quantum nonlinear optics with single photons enabled by strongly interacting atoms, *Nature* **488**, 57 (2012).
  - [12] E. Zeuthen, M. J. Gullans, M. F. Maghrebi, and A. V. Gorshkov, Correlated Photon Dynamics in Dissipative Rydberg Media, *Phys. Rev. Lett.* **119**, 043602 (2017).
  - [13] D. Jaksch, J. I. Cirac, P. Zoller, S. L. Rolston, R. Côté, and M. D. Lukin, Fast Quantum Gates for Neutral Atoms, *Phys. Rev. Lett.* **85**, 2208 (2000).
  - [14] D. S. Weiss, and M. Saffman, Quantum computing with neutral atoms, *Physics Today* **70**, 44 (2017).
  - [15] H. Levine, A. Keesling, G. Semeghini, A. Omran, T. T. Wang, S. Ebadi, H. Bernien, M. Greiner, V. Vuletić, H. Pichler, and M. D. Lukin, Parallel Implementation of High-Fidelity Multiqubit Gates with Neutral Atoms, *Phys. Rev. Lett.* **123**, 170503 (2019).
  - [16] Y. O. Dudin and A. Kuzmich, Strongly Interacting Rydberg Excitations of a Cold Atomic Gas, *Science* **336**, 887 (2012).
  - [17] F. Ripka, H. Kübler, R. Löw, and T. Pfau, A room-temperature single-photon source based on strongly interacting Rydberg atoms, *Science* **362**, 446 (2018).
  - [18] D. P. O'Connell, A. N. Craddock, E. A. Goldschmidt, A. J. Hachtel, Y. Wang, P. Bienias, A. V. Gorshkov, S. L. Rolston, and J. V. Porto, On-demand indistinguishable single photons from an efficient and pure source based on a Rydberg ensemble, *Optica* **7**, 813 (2020).
  - [19] P. Schauß, M. Cheneau, M. Endres, T. Fukuhara, S. Hild, A. Omran, T. Pohl, C. Gross, S. Kuhr, and I. Bloch, Observation of spatially ordered structures in a two-dimensional Rydberg gas, *Nature* **491**, 87 (2012).
  - [20] Y.-Y. Jau, A. M. Hankin, T. Keating, I. H. Deutsch, and G. W. Biedermann, Entangling atomic spins with a Rydberg-dressed spin-flip blockade, *Nature Phys.* **12**, 71 (2016).
  - [21] J. Zeiher, R. van Bijnen, P. Schauß, S. Hild, J.-y. Choi, T. Pohl, I. Bloch, and C. Gross, Many-body interferometry of a Rydberg-dressed spin lattice, *Nature Phys.* **12**, 1095 (2016).
  - [22] H. Labuhn, D. Barredo, S. Ravets, S. de Léséleuc, T. Macrì, T. Lahaye, and A. Browaeys, Tunable two-dimensional arrays of single Rydberg atoms for realizing quantum Ising models, *Nature* **534**, 667 (2016).
  - [23] A. Omran, H. Levine, A. Keesling, G. Semeghini, T. T. Wang, S. Ebadi, H. Bernien, A. S. Zibrov, H. Pichler, S. Choi, J. Cui, M. Rossignolo, P. Rembold, S. Montangero, T. Calarco, M. Endres, M. Greiner, V. Vuletić, and M. D. Lukin, Generation and manipulation of Schrödinger cat states in Rydberg atom arrays, *Science* **365**, 570 (2019).
  - [24] V. Borish, O. Marković, J. A. Hines, S. V. Rajagopal, and M. Schleier-Smith, Transverse-Field Ising Dynamics in a Rydberg-Dressed Atomic Gas, *Phys. Rev. Lett.* **124**, 063601 (2020).
  - [25] D. Bluvstein, A. Omran, H. Levine, A. Keesling, G. Semeghini, S. Ebadi, T. T. Wang, A. A. Michailidis, N. Maskara, W. W. Ho, S. Choi, M. Serbyn, M. Greiner, V. Vuletić, and M. D. Lukin, Controlling quantum many-body dynamics in driven Rydberg atom arrays, *Science* **371**, 1355 (2021).
  - [26] H. Bernien, S. Schwartz, A. Keesling, H. Levine, A. Omran, H. Pichler, S. Choi, A. S. Zibrov, M. Endres, M. Greiner, V. Vuletić, and M. D. Lukin, Probing many-body dynamics on a 51-atom quantum simulator, *Nature* **551**, 579 (2017).
  - [27] S.-S. Hsiao, K.-T. Chen, and I. A. Yu, Mean field theory of weakly-interacting Rydberg polaritons in the EIT system based on the nearest-neighbor distribution, *Opt. Express* **28**, 28414 (2020).
  - [28] B. Kim, K.-T. Chen, S.-S. Hsiao, S.-Y. Wang, K.-B. Li, J. Ruseckas, G. Juzeliūnas, T. Kirova, M. Auzinsh, Y.-C. Chen, Y.-F. Chen, and I. A. Yu, A weakly-interacting many-body system of Rydberg polaritons based on electromagnetically induced transparency, *Commun. Phys.* **4**, 101 (2021).
  - [29] M. Fleischhauer, A. Imamoglu, and J. P. Marangos, Electromagnetically induced transparency: Optics in coherent media, *Rev. Mod. Phys.* **77**, 633 (2005).
  - [30] Y.-W. Lin, H.-C. Chou, P. P. Dwivedi, Y.-C. Chen, and I. A. Yu, Using a pair of rectangular coils in the MOT for the production of cold atom clouds with large optical density, *Opt. Express* **16**, 3753 (2008).
  - [31] B. Kim, K.-T. Chen, C.-Y. Hsu, S.-S. Hsiao, Y.-C. Tseng, C.-Y. Lee, S.-L. Liang, Y.-H. Lai, J. Ruseckas, G. Juzeliūnas, and I. A. Yu, Effect of laser-frequency fluctuation on the decay rate of Rydberg coherence, *Phys. Rev. A* **100**, 013815 (2019).
  - [32] M.-J. Lee, J. Ruseckas, C.-Y. Lee, V. Kudriašov, K.-F. Chang, H.-W. Cho, G. Juzeliūnas, and I. A. Yu, Experimental demonstration of spinor slow light, *Nat. Comm.* **5**, 5542 (2014).
  - [33] I. I. Beterov, I. I. Ryabtsev, D. B. Tretyakov, and V. M. Entin, Quasiclassical calculations of blackbody-radiation-induced depopulation rates and effective lifetimes of Rydberg  $nS$ ,  $nP$ , and  $nD$  alkali-metal atoms with  $n \leq 80$ , *Phys. Rev. A* **79**, 052504 (2009); Erratum,

- Phys. Rev. A **80**, 059902(E) (2009).
- [34] D. A. Steck, Rubidium 87 D Line Data, available online at <http://steck.us/alkalidata> (Version 2.2.2, last revised 9 July 2021).
  - [35] T. G. Walker and M. Saffman, Consequences of Zeeman degeneracy for the van der Waals blockade between Rydberg atoms, Phys. Rev. A **77**, 032723 (2008).
  - [36] K. Afrousheh, P. Bohlouli-Zanjani, D. Vagale, A. Muford, M. Fedorov, and J. D. D. Martin, Spectroscopic Observation of Resonant Electric Dipole-Dipole Interactions between Cold Rydberg Atoms, Phys. Rev. Lett. **93**, 233001 (2004).
  - [37] E. A. Goldschmidt, T. Boulier, R. C. Brown, S. B. Koller, J. T. Young, A. V. Gorshkov, S. L. Rolston, and J. V. Porto, Anomalous Broadening in Driven Dissipative Rydberg System, Phys. Rev. Lett. **116**, 113001 (2016).
  - [38] T. Boulier, E. Magnan, C. Bracamontes, J. Maslek, E. A. Goldschmidt, J. T. Young, A. V. Gorshkov, S. L. Rolston, and J. V. Porto, Spontaneous avalanche dephasing in large Rydberg ensembles, Phys. Rev. A **96**, 053409 (2017).
  - [39] J. de Hond, N. Cisternas, R. J. C. Spreeuw, H. B. van Linden van den Heuvell, and N. J. van Druten, Interplay between van der Waals and dipole-dipole interactions among Rydberg atoms, J. Phys. B: At. Mol. Opt. Phys. **53**, 084007 (2020).
  - [40] P. Bienias, J. Douglas, A. Paris-Mandoki, P. Titum, I. Mirgorodskiy, C. Tresp, E. Zeuthen, M. J. Gullans, M. Manzoni, S. Hofferberth, D. Chang, and A. V. Gorshkov, Photon propagation through dissipative Rydberg media at large input rates, Phys. Rev. Research **2**, 033049 (2020).
  - [41] C. Ates, T. Pohl, T. Pattard, and J. M. Rost, Antiblockade in Rydberg Excitation of an Ultracold Lattice Gas, Phys. Rev. Lett. **98**, 023002 (2007).
  - [42] T. Amthor, C. Giese, C. S. Hofmann, and M. Weidemüller, Evidence of Antiblockade in an Ultracold Rydberg Gas, Phys. Rev. Lett. **104**, 013001 (2010).
  - [43] A. Derevianko, P. Kómár, T. Topcu, R. M. Kroeze, and M. D. Lukin, Effects of molecular resonances on Rydberg blockade, Phys. Rev. A **92**, 063419 (2015).
  - [44] T. J. Carroll, K. Claringbould, A. Goodsell, M. J. Lim, and M. W. Noel, Angular Dependence of the Dipole-Dipole Interaction in a Nearly One-Dimensional Sample of Rydberg Atoms, Phys. Rev. Lett. **93**, 153001 (2004).
  - [45] A. Reinhard, T. Cubel Liebisch, K. C. Younge, P. R. Berman, and G. Raithel, Rydberg-Rydberg Collisions: Resonant Enhancement of State Mixing and Penning Ionization, Phys. Rev. Lett. **100**, 123007 (2008).
  - [46] M. Eder, A. Lesak, A. Plone, T. Yoda, M. Highman, and A. Reinhard, Quantifying the impact of state mixing on the Rydberg excitation blockade, Phys. Rev. Research **2**, 023234 (2020).
  - [47] A. André, M. Bajcsy, A. S. Zibrov, and M. D. Lukin, Nonlinear Optics with Stationary Pulses of Light, Phys. Rev. Lett. **94**, 063902 (2005).
  - [48] Y.-W. Lin, W.-T. Liao, T. Peters, H.-C. Chou, J.-S. Wang, H.-W. Cho, P.-C. Kuan, and I. A. Yu, Stationary Light Pulses in Cold Atomic Media and without Bragg Gratings, Phys. Rev. Lett. **102**, 213601 (2009).
  - [49] J. L. Everett, D. B. Higginbottom, G. T. Campbell, P. K. Lam, and B. C. Buchler, Stationary Light in Atomic Media, Adv. Quantum Technol. **2**, 1800100 (2019).
  - [50] M. Fleischhauer, J. Otterbach, and R. G. Unanyan, Bose-Einstein Condensation of Stationary-Light Polaritons, Phys. Rev. Lett. **101**, 163601 (2008).